Chemical Geology 726 (2026) 123744

Contents lists available at ScienceDirect

Chemical Geology

journal homepage: www.elsevier.com/locate/chemgeo

Research Paper

Volcanic sourced input enhances biological export in the Kuroshio Extension

Zenghui Zhu [a,b,c,d], Pinghe Cai [e], Qian Liu [a,b], Wen Liu [a,b,c], Xueyan Jiang [a,b], Xiaoyi Guo [a,b,c], Shibin Zhao [a,b,c], Wenkai Guan [f], Honghai Zhang [a,b], Guangchao Zhuang [a,b], Ergang Lian [g], Shuo Ren [a,b,c], Ran An [a,b,c], Shanshan Chen [a,c], Zhaohui Chen [h], Bochao Xu [a,b,*]

[a] Frontiers Science Center for Deep Ocean Multispheres and Earth System, and Key Laboratory of Marine Chemistry Theory and Technology, Ministry of Education, Ocean University of China, Qingdao 266100, PR China
[b] Laboratory for Marine Ecology and Environmental Science, Qingdao Marine Science and Technology Center, Qingdao 266100, PR China
[c] College of Chemistry and Chemical Engineering, Ocean University of China, Qingdao 266100, PR China
[d] Academy of the Future Ocean, Ocean University of China, Qingdao 266100, PR China
[e] State Key Laboratory of Marine Environmental Sciences, College of Ocean and Earth Sciences, Xiamen University, Xiamen 361005, PR China
[f] School of Oceanography, Shanghai Jiao Tong University, Shanghai 200030, PR China
[g] Ecological Environment Monitoring and Scientific Research Center, Taihu Basin & East China Sea Ecological Environment Supervision and Administration Bureau, Ministry of Ecology and Environment, Shanghai 200125, China
[h] College of Oceanic and Atmospheric Sciences, Ocean University of China, Qingdao 266100, PR China

ARTICLE INFO

Editor: Don Porcelli

Keywords:
Aeolian dust
Volcanic ash
Fe input
Biological export
^{230}Th normalization

ABSTRACT

The Kuroshio Extension lies at the confluence of the North Pacific subtropical and subarctic gyres and receives particulate inputs from Asian dust and volcanic arcs. Constraining the provenance and burial fluxes of these materials is key to understanding how external nutrient supply regulates oceanic productivity. Here we quantify mass fluxes and sediment source contributions across a north–south transect of five sediment cores, using a combined approach of ^{230}Th profile dating and ^{230}Th normalization. Mass flux shows a pronounced north-to-south gradient, decreasing from 2.7 g cm^{-2} ka^{-1} in the north to 0.38 g cm^{-2} ka^{-1} in the south. Aeolian dust provides a regionally uniform lithogenic flux (0.18–0.25 g cm^{-2} ka^{-1}), whereas volcanic inputs are more localized but more potent, with fluxes ranging from 0.06 to 1.72 g cm^{-2} ka^{-1}. Volcanic flux co-varies spatially with biogenic–authigenic burial flux ($r = 0.78$), and elevated volcanic inputs in the northern cores are accompanied by enhanced burial of biogenic and authigenic materials (0.07–0.75 g cm^{-2} ka^{-1}) This pattern suggests that volcanic iron fertilization may enhance biological export and promote the co-sequestration of trace metals such as rare earth elements. Our findings show that aeolian dust supplies a background level of trace metals, while volcanic inputs drive localized hotspots of biological productivity and metal burial. This framework highlights the interconnected roles of lithogenic sources in regulating the biological pump, although direct constraints on iron bioavailability await further investigation.

1. Introduction

Marine sediments serve as major reservoirs for particles and trace metals, although they can also act as sources via early diagenetic remobilization and benthic fluxes (e.g., Du et al., 2025). Understanding their burial fluxes is essential for constraining the net sink strength and evaluating the long-term sequestration of these elements. The primary sources of marine sediments include atmospheric dust, volcanogenic materials, and biogenic and authigenic components. The Kuroshio Extension, situated in the western North Pacific, is characterized by high biological productivity and dynamic oceanic processes. This region thus provides an ideal natural laboratory to investigate particle sources, burial fluxes, and their controlling mechanisms (Nishioka et al., 2020).

Iron (Fe) limitation is widely recognized as a major factor constraining phytoplankton growth in the open ocean (Martin and Fitzwater, 1988; Serno et al., 2014a; Burgay et al., 2021). Aeolian

* Corresponding author at: Frontiers Science Center for Deep Ocean Multispheres and Earth System, and Key Laboratory of Marine Chemistry Theory and Technology, Ministry of Education, Ocean University of China, Qingdao 266100, PR China.
E-mail address: xubc@ouc.edu.cn (B. Xu).

https://doi.org/10.1016/j.chemgeo.2026.123744
Received 30 April 2026; Received in revised form 23 September 2026; Accepted 28 September 2026
Available online 29 September 2026
0009-2541/© 2026 Elsevier B.V. All rights are reserved, including those for text and data mining, AI training, and similar technologies.

dust and volcanic ash are potential sources of Fe to surface waters and are thus important for understanding trace metal cycling and biological productivity (Mahowald et al., 2018; Olgun et al., 2011). Mineralogical analyses of bulk sediments and atmospheric dust (Letelier et al., 2019; Kurisu et al., 2021; Crusius et al., 2024; Wang et al., 2025b) indicate that aerosols from central Asian arid and semi-arid regions are transported and deposited into the surface waters of the Northwest Pacific, serving as a key Fe source (Zan et al., 2025). The role of volcanic ash in surface ocean biogeochemical Fe cycling has remained poorly quantified, though increasing evidence (Hamme et al., 2010; Olgun et al., 2011; Lam et al., 2012, 2013) highlight its potential significance and suggest that volcanic ash inputs may be comparable to, or even regionally exceed, those of lithogenic dust.

Unlike aeolian dust and volcanic materials, biogenic and authigenic particles come mainly from biological production in the upper ocean. These include bioapatite fossils and Fe-Mn micronodules, and they serve as important sinks for trace metals (Liao et al., 2022; Xiao et al., 2024; Wang et al., 2025a). Previous studies have focused mostly on REE-enriched depositional regions, showing that biological export can enrich trace metals in areas with low sedimentation rates (Liao et al., 2022). However, how biogenic–authigenic minerals contribute to trace metal burial in high-sedimentation-rate settings remains poorly understood.

A key challenge is to separate and quantify these different sources, since they are mixed together in bulk sediments. Various chemical and physical separation techniques have been developed to address this, including sequential extraction, geochemical tracers (e.g., REEs, Sr-Nd isotopes, ^{4}He-^{232}Th systematics), and statistical methods such as end-member mixing analysis (Olivarez et al., 1991; Weber II et al., 1996; Ziegler et al., 2007; Jiang et al., 2013; Seo et al., 2014; Zhao et al., 2019; Crusius et al., 2024).

These advances have greatly improved our understanding of sediment provenance in the North Pacific. Previous studies show that volcanic materials dominate near volcanic arcs, such as the Kuril and Aleutian Islands, whereas aeolian dust dominates in the central and eastern Pacific (Weber II et al., 1998; Ziegler et al., 2007). Serno et al. (2014a) conducted an extensive core-top survey across the Subarctic North Pacific, using geochemical proxies to map the spatial distribution of aeolian dust and volcanic contributions to surface sediments. Notably, they observed that biogenic barium fluxes correlate moderately with export production in the central and eastern Subarctic North Pacific, yet exhibit no significant correlation in the western sector—a regional discrepancy that remains mechanistically unexplained (Serno et al., 2014b). The Kuroshio Extension lies at the boundary between the subtropical and subarctic gyres and exhibits a sharp north–south contrast in productivity. However, the provenance of sedimentary materials across this gradient—and the respective roles of Asian dust versus volcanic inputs—has received comparatively little attention.

Quantifying mass flux—the flux of material from the water column to the seafloor—is another key challenge. This metric provides insight into upper ocean processes that are fundamental to Earth system functioning (Francois et al., 2004; Costa et al., 2024). Despite its importance, mass flux in the subarctic open ocean remains poorly constrained, largely due to methodological difficulties. High sedimentation rates hinder the use of traditional geochronological tools over geological timescales, and deep depths (below the carbonate compensation depth) limit the preservation of foraminiferal shells needed for radiocarbon dating (Hayes et al., 2021).

The development of ^{230}Th-based techniques has opened new possibilities for constraining sediment accumulation in regions where traditional dating methods fail. Costa et al. (2024) recently applied ^{230}Th depth profiling to constrain average sedimentation rates over the past 500 ka across the deep (>3000 m) North Pacific, revealing low rates (<0.25 cm ka^{-1}) in the subtropical gyre and elevated rates (>0.5 cm ka^{-1}) between 30° and 40°N, particularly west of 160°W. Their study establishes a valuable chronological framework for the region, but does not resolve sediment provenance or biogeochemical fluxes. Serno et al. (2014a) applied ^{230}Th normalization to constrain mass fluxes in the Subarctic North Pacific, but this approach conventionally requires an independent chronology to decay-correct the excess ^{230}Th activity. In our study area, such age constraints are scarce owing to poor carbonate preservation. We therefore adopt an integrated framework combining ^{230}Th profile dating with ^{230}Th normalization, which enables mass flux reconstruction without recourse to ^{14}C or δ^{18}O chronologies.

Here, we combine ^{230}Th profile dating with ^{230}Th normalization to derive reliable mass fluxes, and integrate these with sequential extraction data to: (1) quantify the burial fluxes of different sediment components (aeolian dust, volcanic material, and biogenic-authigenic particles), and (2) examine how the input of volcanic material relates to enhanced biological export and trace metal burial.

2. Samples and methods

2.1. Study area and sampling

The Kuroshio Extension is situated in the western North Pacific. This region is characterized by high primary productivity, markedly exceeding that of typical oligotrophic open-ocean regions. This dynamic system receives dual terrigenous inputs, from both Asian aeolian dust and volcanic materials derived from the Northeast Asian island arcs. In addition, the accumulation of substantial amounts of biogenic and authigenic minerals influences the burial and geochemical behavior of trace metals in the sediments.

Sediment cores samples were collected onboard of R/V *dongfanghong 3* implementing the open research cruise NORC2024-584 (stations were shown in Supplementary materials Table S1 and Fig. 1a). Sediment core samples were collected using a box corer to minimize surface disturbance and preserve the integrity of the sediment-water interface. After retrieval, the cores were sectioned at 1 cm intervals, and the samples were frozen and stored in plastic bags for subsequent geochemical analyses.

2.2. Sequential leaching

A sequential leaching procedure was employed to chemically fractionate Fe, Mn, and REEs into operationally defined phases. Our procedure is adapted from established protocols, including the Tessier method (Tessier et al., 1979), the three-step sequential extraction scheme of the European Community Bureau of Reference (BCR; Nemati et al., 2011), and sequential leaching schemes developed for deep-sea sediments (Koschinsky and Halbach, 1995; Liao et al., 2022; Xiao et al., 2024). The material remaining after the sequential extraction is termed as the 'residual' component. We note that this 'residual' component is operationally defined by the extraction protocol (Ziegler et al., 2007), and this terminology is used throughout the paper. The sequential extraction steps are briefly listed in Table 1.

2.3. Sediment digestion and chemical analyses

For the analysis of major, minor, and trace elements (including Al, Fe, Mn, ^{232}Th, ^{238}U, and REEs), approximately 100 mg of finely ground (<200 mesh) sediment sample was subjected to total digestion. Digestion was performed using a mixture of concentrated HNO_3, $HClO_4$, and HF (5:2:2, *v*/v/v) in tightly sealed Teflon PFA screw-cap vessels placed on a hotplate at 180 °C for 48 h. After complete digestion, the vessels were opened, and the solutions were evaporated on a hotplate at 160 °C until near dryness to remove HF and $HClO_4$. The residues were then dissolved in 2% (*v*/v) high-purity HNO_3 and diluted to a known mass for analysis. Elemental concentrations were determined using an inductively coupled plasma mass spectrometer (ICP-MS; Thermo Scientific iCAP Q), following analytical procedures detailed in Guan et al. (2026). Potential spectral interferences, such as barium oxide (BaO^+) on

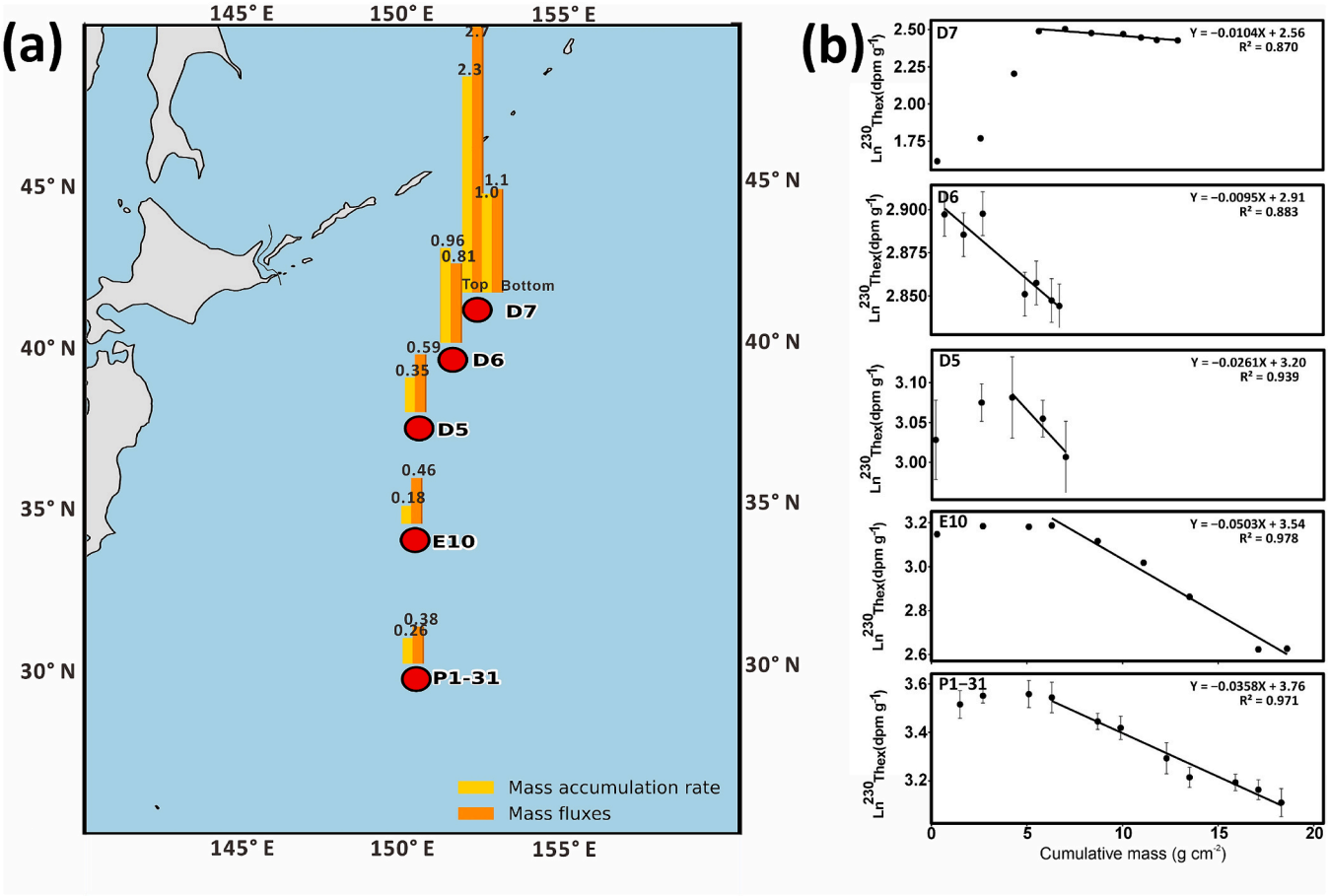


Fig. 1. (a) Spatial distribution of mass accumulation rates (MAR, g cm^{-2} ka^{-1}) and ^{230}Th-normalized mass fluxes (g cm^{-2} ka^{-1}). (b) Vertical profiles of ^{230}Th activity at the five stations.

Table 1
Details of the sequential leaching scheme of sediments.

Step	Associated phase	Extractant	pH
1	Exchangeable	25 mL 1 M $MgCl_2$, 24 h	8.7
2	Calcium carbonate/Calcium phosphate	25 mL 1 M Na-acetate, 24 h	4.5
3	Easily reducible Fe-Mn-oxides	25 mL 0.1 M hydroxylamine-HCl, 2 h	2.0
4	Oxidizable fraction	10 mL 8.8 M H_2O_2, 2 h then 25 ml 1 M ammonium acetate, 16 h	3.5
5	Biogenic silica	25 mL 2 M sodium carbonate, 8 h	
Residue	Aluminosilicate	Total digestion with $HClO_4$, HNO_3, and HF, 48 h	

europium isotopes ($^{151}Eu^+$, $^{153}Eu^+$), were monitored and corrected for using interference equations and by analyzing single-element standard solutions.

Analytical accuracy and precision were assessed by analyzing a certified stream sediment reference material (GSD-9, Institute of Geophysical and Geochemical Exploration, Chinese Academy of Geological Sciences). For elements with certified values, replicate analyses ($n = 6$) generally fell within the certified uncertainty ranges. The relative standard deviation (RSD) was typically better than 10%. Measured concentrations from the GSD-9 replicates and the certified reference values are given in Supplementary Table S6. All acids used were of trace metal grade (Fisher Scientific). All aqueous solutions were prepared using 18.2 MΩ·cm deionized water (Milli-Q, Millipore). To verify the reliability and completeness of the sequential extraction procedure, an internal mass balance check was performed. For each element, the sum of the concentrations recovered in all sequential leaching steps (Steps 1–5 plus the residual fraction) was compared to the concentration obtained from direct total digestion of a separate aliquot of the bulk sediment. For the key elements of interest (Fe, Mn, Al, and ΣREE), recoveries ranged from 90% to 110%, confirming the robustness and reproducibility of the sequential extraction scheme.

2.4. Radiochemical measurements

The measurement of ^{230}Th activity in sediments followed established radiochemical separation and isotopic dilution methods, as detailed in Cheng et al. (2024). Briefly, a separate aliquot of approximately 100 mg of freeze-dried, homogenized sediment was accurately weighed into a pre-cleaned Teflon vessel. The ^{229}Th tracer solution with known activity (~5.0 dpm) was added to each sample for isotopic dilution quantification. The sediment digestion procedure was similar to the total digestion method described in Section 2.3. Thorium was then separated and purified from the sample matrix using classic anion-exchange chromatography (AG 1 × 8, 100–200 mesh), following established protocols (Anderson and Fleer, 1982; Yuan et al., 2023). The purified Th fraction was evaporated and redissolved in 2 mL of 2% (*v*/v) high-purity HNO_3 for measurement. ^{230}Th/^{229}Th ratios were measured using a high-resolution ICP-MS (Element XR, Thermo Fisher Scientific) equipped with an Apex-Q desolvating nebulizer and a high-sensitivity Jet interface. Measurements were conducted at the State Key Laboratory of Marine Environmental Science of Xiamen University. The procedural blank for ^{230}Th was negligible compared to sample signals. Based on repeated measurements of standards and sample replicates, the external

reproducibility for $^{230}Th/^{229}Th$ ratios was better than 1.0% (±1σ) for samples with sufficient signal intensity.

2.5. Mass flux quantification model

Over recent decades, ^{230}Th normalization has been established as a standard approach for reconstructing past mass fluxes (particle rain rates) in marine sedimentary records (Francois et al., 2004; Costa et al., 2020). Thorium ($t_{1/2}$ = 75,400 y) is highly particle-reactive and insoluble in seawater, in contrast to its parent isotope, uranium. The ^{230}Th produced in situ by the radioactive decay of dissolved ^{234}U is rapidly scavenged from the water column via adsorption onto sinking particles (Bacon and Anderson, 1982). The residence time of thorium in seawater is short and depth-dependent, ranging from less than a few years in surface waters to several decades in deep waters (Anderson and Fleer, 1982). This short residence time relative to ocean mixing timescales ensures that ^{230}Th removal and deposition reflect primarily vertical particle flux from the overlying water column, with minimal bias from lateral sediment transport.

The total ^{230}Th activity, $(^{230}Th)_T$, in deep-sea sediments comprises three principal components:

(a) Excess ^{230}Th activity, $(^{230}Th)_{ex}$: The fraction scavenged from the overlying water column and delivered to the seafloor. This unsupported component, which disturbs the secular equilibrium between ^{230}Th and its parent ^{234}U in the sediment, forms the basis for flux normalization.
(b) Detrital ^{230}Th activity, $(^{230}Th)_{det}$: The ^{230}Th supported by its parent ^{238}U within the crystal lattice of detrital (lithogenic) minerals. This component is inherited from the continental crust and introduced via terrigenous (aeolian, volcanic) inputs.
(c) Authigenic ^{230}Th: ^{230}Th produced within the sediment column by the decay of ^{234}U that has diffused from the overlying water under reducing (anoxic) porewater conditions. In oxic depositional environments, this contribution is considered negligible (Francois et al., 2004).

Under oxic conditions, assuming secular equilibrium within the detrital fraction, the supported (detrital) ^{230}Th activity is equal to the activity of its ultimate parent ^{238}U:

$$\left(^{230}Th\right)_{det} = \left(^{238}U\right)$$

The excess (or unsupported) ^{230}Th activity, representing the scavenged water-column-derived component, is then calculated as:

$$\left(^{230}Th\right)_{ex} = \left(^{230}Th\right)_{T} - \left(^{230}Th\right)_{det}$$

The ^{230}Th-normalized mass flux (F, in the unit of g m^{-2} yr^{-1}) is then calculated as (Francois et al., 2004; Costa et al., 2020):

$$F = \frac{\beta z}{\left(^{230}Th\right)_{ex,0}}$$

where β is the exactly known production rate of ^{230}Th (0.0267 dpm m^{-3} yr^{-1}, Francois et al., 2004). z is water depth (m). The term β z is equivalent to the integrated ^{230}Th production in the overlying water column. $(^{230}Th)_{ex,0}$ is the decay-corrected initial excess ^{230}Th activity in the surface sediment (dpm g^{-1}).

A critical requirement of this method is an independent chronology to correct $A_{230Thex0}$ for radioactive decay since the time of deposition. Such chronologies are often derived from oxygen isotope stratigraphy or radiocarbon (^{14}C) dating. In the absence of reliable age models, applying ^{230}Th normalization is significantly limited.

To overcome this limitation, we employed a two-step approach: (1) we first used the depth profile of excess ^{230}Th to establish a mass accumulation rate (MAR)-based chronology following the constant flux-constant sedimentation rate model (Sanchez-Cabeza and Ruiz-Fernández, 2012, or a modified iterative model for station D7; see Section 3.1.1). ^{230}Th, with its strong affinity for particles, can also serve as a tool for dating deep-sea sediments (e.g., Geibert et al., 2019; Cheng et al., 2024). Unlike the ^{230}Th-normalization, which corrects for sediment redistribution, ^{230}Th dating based on a decay profile provides an estimate of the total MAR at a specific site, regardless of sediment redistribution. Instead, it provides an estimate of the mass accumulation rate. (2) we then applied this chronology to decay-correct the surface sediment $^{230}Th_{ex}$ activity and compute the ^{230}Th-normalized mass flux. This integrated approach, while building on established principles, represents a novel application that extends the utility of ^{230}Th to sedimentary environments where traditional dating methods are not feasible.

2.6. Particle composition proportions quantification

In this study, the lithogenic fraction (FL) and biogenic fraction of the sediment were quantified using aluminum (Al) content as a conservative terrigenous proxy. Al is primarily derived from continental sources and exhibits oceanic residence time on the order of decades. Its conservative behavior in marine settings—meaning it is largely unaffected by biogeochemical processes after deposition—makes it a robust and widely adopted proxy for normalizing sedimentary element concentrations and correcting for variable dilution by biogenic material (McKay and Pedersen, 2008). Consequently, the measured Al content broadly represents the total terrigenous flux and can be used to reliably calculate the proportion of lithogenic material within the bulk sediment (Shigemitsu et al., 2007).

The lithogenic fraction and biogenic fraction of the sediments were estimated using Al as a conservative terrigenous proxy according to the formula:

$$FL = \frac{[Al]_{Sample}}{[Al]_{Lithogenic}}$$

$$\text{Biogenic fraction} = 1 - FL$$

where $[Al]_{sample}$ is the measured Al concentration in sediments, and $[Al]_{lithogenic}$ is the reference Al concentration in average upper continental crust (8.15%; Rudnick and Gao, 2014). This approach assumes that all Al is of terrigenous origin and that its crustal abundance is relatively uniform, which is well-supported for marine sediments (McKay and Pedersen, 2008).

We used different geochemical proxies (^{232}Th and REEs, measured in sediment samples and sequential leaching samples) combined with information about dust and volcanic endmembers to determine the dust and volcanic fraction of each sample.

2.6.1. Th approaches

The concentration of Th was utilized to quantitatively apportion the relative contributions of aeolian dust and volcanic material. Th is particularly effective in distinguishing different source materials due to its notable depletion in volcanic arc components compared to upper continental crust and aeolian dust (Weber II et al., 1996). Representative end-member compositions were defined based on literature values: Asian aeolian loess (Th = 14.6 ± 1.03 μg g^{-1}), approximating the upper continental crust (Taylor and McLennan, 1985), and typical North Pacific volcanic arc material (Th = 1.9 ± 0.95 μg g^{-1}; Weber II et al., 1996), which is based on the average ash composition from ODP Leg 145 Sites 881–884, together with Kurile–Kamchatka volcanic material and Kurile island-arc material. These values are consistent with regional provenance studies (e.g., Serno et al., 2014a).

It is important to note that Th concentrations in aeolian dust vary with grain size, and are generally higher in fine-grained fractions (<4 or < 5 μm; McGee et al., 2016). Because of aerodynamic sorting, long-

range transported Asian dust reaching the remote North Pacific is dominated by fine clay and fine silt particles (Duce et al., 1991; Maeda et al., 2007). Recent aerosol observations in the western North Pacific also support a fine-grained, Th-enriched Asian dust signature (Wang et al., 2025b). The Th end-member we use (14.6 μg g^{-1}) falls within the range of 14 ± 1 μg g^{-1} recommended by McGee et al. (2016) for fine-grained Asian dust, so it is a reasonable approximation for the aeolian fraction deposited in our study area. However, using a single end-member value is a simplification and remains a source of uncertainty.

The fractional contributions were calculated using a simple binary mixing model (Weber II et al., 1996):

$$f_{dust} = \frac{[Th]_{sample} - [Th]_{volcanic}}{[Th]_{dust} - [Th]_{volcanic}} \times FL$$

$$f_{\mathrm{volcanic}} = FL - f_{\mathrm{dust}}$$

where f_{dust} and f_{volcanic} are the dust and volcanic fraction, $[Th]_{\mathrm{sample}}$ is the measured Th concentration in the sediment sample (μg g^{-1}). $[Th]_{\mathrm{dust}}$ and $[Th]_{\mathrm{volcanic}}$ are the characteristic Th concentrations for the defined dust end-member (14.6 μg g^{-1}) and volcanic end-member (1.9 μg g^{-1}).

2.6.2. Residual-phase REEs approaches

The REE signatures in bulk sediments can be significantly altered by secondary processes such as adsorption from seawater, diagenetic remobilization, and incorporation into authigenic phases. Therefore, to accurately extract and quantify the relative contributions of detrital sources-particularly aeolian dust and volcanogenic inputs—it is essential to isolate the REEs least affected by these modifications. The residual phase was emphasized because its REE fractionation patterns are considered to most faithfully preserve the original terrigenous and volcanic signals, with minimal overprinting from diagenesis or seawater interaction. Consequently, we used the REE patterns (specifically the La/Yb ratio) of the residual fraction to apportion the terrigenous flux between aeolian and volcanic end-members.

To quantify these contributions, a simple two-endmember mixing model based on the La/Yb ratio was applied to the residual fraction (Otosaka et al., 2004; Maeda et al., 2007). Representative La/Yb values for the end-members were taken from the literature: La/Yb = 14.56 for Asian loess (< 4.2 μm) and La/Yb = 3.4 for typical North Pacific volcanic arc material (Bailey, 1993; Weber II et al., 1996; Shigemitsu et al., 2007). This value is similar to the tholeiitic series volcanic rocks of the Aleutians reported by Kay (1977). Absolute REE concentrations in Asian dust can vary with source region, transport pathway, and grain size (Jeong, 2020). Still, PAAS-normalized REE patterns and key elemental ratios such as La/Yb tend to be more stable than absolute concentrations and generally resemble upper continental crust compositions (Zhang et al., 2016). Using the residual-phase La/Yb ratio therefore reduces (but does not eliminate) uncertainty from variations in absolute concentrations.

The dust fraction in the terrigenous component was calculated as:

$$(La/Yb)_{Sample} = \left[(La/Yb)_{dust} f_{dust} + (La/Yb)_{volcanic} f_{volcanic}\right] \Big/ FL$$

$$f_{\mathrm{volcanic}} = FL - f_{\mathrm{dust}}$$

where $(La/Yb)_{\mathrm{Sample}}$ is the measured ratio in the sediment residual fraction. $(La/Yb)_{\mathrm{volcanic}}$ and $(La/Yb)_{\mathrm{dust}}$ are the characteristic La/Yb. The calculation method of the volcanic fraction is the same as that of the Th approaches.

2.7. Calculation of trace metal flux in different forms

The burial flux of each trace metal species (e.g., Fe in Fe-Mn oxides, REEs in the biogenic and authigenic fraction) was calculated by multiplying its concentration (μg g^{-1}) in the respective operationally defined phase (from sequential extraction) by the total ^{230}Th-normalized mass flux (g cm^{-2} ka^{-1}) at each station.

3. Results

3.1. Sediment mass fluxes constrained by ^{230}Th

3.1.1. Spatial patterns of mass accumulation rates (MARs) derived from $^{230}Th_{ex}$ profiles

Sediment cores from the southern stations (E10 and P1–31) exhibit relatively constant excess ^{230}Th activity, $(^{230}\mathrm{Th})_{\mathrm{ex}}$ in the upper ~10 cm, followed by a gradual decrease with depth (Fig. 1b). A surface mixed layer with homogeneous $(^{230}\mathrm{Th})_{\mathrm{ex}}$ activity is characteristic of deep-sea sediments. This feature is typically attributed to the continuous supply of ^{230}Th to the seafloor via particle scavenging from the water column, combined with modern effective bioturbation that homogenizes the high ^{230}Th signal within the surface sediment layer (Cochran and Krishnaswami, 1980). Below ~10 cm, the ^{230}Th activity profiles show clear exponential decay.

In contrast, cores from northern stations D5, D6, and D7 below 12 cm show minimal variation in $^{230}\mathrm{Th}_{\mathrm{ex}}$ activity (typically <1 dpm g^{-1}; Fig. 1b). This weak signal is likely due to a combination of shorter core lengths and higher sedimentation rates. Although the decay trend in these profiles is weak, the high precision of the ^{230}Th measurements (relative standard deviation <3%) still allows reliable fitting of the profiles and estimation of MARs and mass fluxes. We adopted the constant flux-constant sedimentation rate (CF-CS) model for sedimentation rate estimation. We applied the model to cumulative mass depth (g cm^{-2}) rather than absolute depth to account for sediment compaction and downcore variations in dry bulk density.

At station D7, the upper 0–12 cm shows a pronounced reversed vertical trend in $^{230}\mathrm{Th}_{\mathrm{ex}}$ activity (Fig. 1b). Meanwhile, ^{232}Th activity decreases from 0.08 dpm g^{-1} at the surface to 0.03 dpm g^{-1} at 16.5 cm depth (Supplementary materials Table S2). The corresponding variations in dry bulk density and mean grain size (Supplementary materials Table S3) indicate a significant and progressive shift in mineral composition. These changes imply an increased influx of fine-grained, ^{232}Th-rich terrigenous material, which diluted the scavenged, seawater-derived ^{230}Th signal. This alteration rendered the standard CF-CS model inapplicable to the upper 12 cm. Consequently, we developed a revised model to address this issue. The model is based on two key assumptions: (1) the flux of excess ^{230}Th $(^{230}\mathrm{Th})_{\mathrm{ex}}$ to the sediment-water interface remained constant over the relevant timescales, and (2) the initial concentration of $^{230}\mathrm{Th}_{\mathrm{ex}}$ in the particulate matter is inversely proportional to the MAR. These assumptions are reasonable given the short residence time of ^{230}Th in the water column and its rapid removal to the seafloor via proximal scavenging (Francois et al., 2004).

We initialized the model using the measured, non-decay-corrected $^{230}\mathrm{Th}_{\mathrm{ex}}$ activity profile and the constant MAR from depths below 12 cm. An iterative procedure was then used to resolve the interdependence between MAR and depositional age. In each iteration, we calculated MAR and age for each layer, decay-corrected the $(^{230}\mathrm{Th})_{\mathrm{ex}}$ activities, and used the corrected profile for the next iteration. This process continued until the MAR values converged to stable solutions.

As shown in Fig. 1a, the highest MAR (2.3 ± 0.5 g cm^{-2} ka^{-1}) was observed in the surface layer of station D7, then decreased gradually to 1.0 ± 0.2 g cm^{-2} ka^{-1} at 12 cm depth and remained relatively constant below. Stations D6 and D7 in the north exhibited the highest MAR values, with a general decreasing trend from north to south. In contrast, the southern stations E10 and P1–31 had much lower MAR values, at 0.18 ± 0.01 and 0.26 ± 0.02 g cm^{-2} ka^{-1}, respectively. For stations D5, D6, E10, and P1–31, no significant downcore variations in MAR were observed.

The MAR values at E10 and P1–31 are consistent with earlier results from this area (Yang et al., 1986) and with recent compilations from other parts of the North Pacific (Costa et al., 2024). Our study provides

the first reported sedimentation rates for the deep-sea plains in the mixed zone and the Oyashio-influenced region of the northern Kuroshio Extension. We observed a clear north-to-south gradient in MAR, with values varying by more than an order of magnitude. Possible drivers of this spatial gradient are discussed in the following section.

3.1.2. Spatial patterns of ^{230}Th-normalized mass fluxes

The MAR calculations described above provide a robust chronological framework. We then derived ^{230}Th-normalized mass fluxes using the method in Section 2.5. Overall, the spatial patterns of MAR and ^{230}Th-normalized mass flux are similar (Fig. 1a), and the results from the two methods are consistent ($r = 0.96$).

The relative difference between the two is more pronounced at the southern stations (E10 and P1–31), where sedimentation rates are low, exceeding analytical uncertainty. We see two possible explanations. One is sediment focusing or winnowing by bottom currents. At lower sedimentation rates, sediments are exposed to reworking by bottom currents and bioturbation for longer periods, which may amplify focusing or winnowing effects. The other is that initial $^{230}Th_{ex}$ activity may be underestimated due to biological mixing. At the southern stations, lower sedimentation rates allow more ^{230}Th decay within the sediment column, so older sediment gets mixed into younger layers, diluting the ^{230}Th signal and thus overestimating the ^{230}Th-normalized mass flux. Our previous work in this region documented excess ^{210}Pb activities extending to depths of ~10 cm (Zhu et al., 2024), indicating that sediment deposited over the last decades has been mixed into older layers (over 10 thousand years old). In contrast, at northern stations D6 and D7, sedimentation is rapid enough that ^{230}Th decay within the sediment is negligible. Under these conditions, MAR from the $^{230}Th_{ex}$ decay profile agrees more closely with the ^{230}Th-normalized mass flux.

3.2. Geochemical composition and source discrimination

3.2.1. Bulk sediment geochemistry and REE patterns

Significant temporal variations in bulk geochemical composition were observed only at station D7. For station D7, the core was divided into two intervals: the surface section (0–12 cm), representing recent deposition, and the deeper section (>12 cm), characterized by a stable sedimentation rate.

The Post-Archean Australian average shale (PAAS)-normalized REE patterns (Taylor and McLennan, 1985) provide insights into the sediment provenance and depositional processes in the Kuroshio Extension region (Supplementary Table S4, S5). A slight enrichment of medium REEs (MREE) is observed at stations D6 and P1–31. Their REE patterns are similar to those of Asian loess (Weber II et al., 1998). This similarity suggests a dominant source contribution of aeolian dust at these stations. In contrast, sediments from the northern stations exhibit notable enrichment in heavy REEs (HREE). This is particularly pronounced in the surface sediments (0–5 cm) of station D7, which have a low La/Yb ratio of 4.1 ± 0.1. This ratio is much lower than the typical loess signature (La/Yb = 13.6, Weber II et al., 1996), but closer to values characteristic of volcanogenic materials, such as debris from the Kuril-Kamchatka arc (La/Yb = 3.41; Weber II et al., 1998). This HREE enrichment may reflect enhanced input of HREE-rich volcaniclastic material from northern sources (Censi et al., 2007), or intensified formation of authigenic minerals under high-productivity conditions, which preferentially incorporate REEs from seawater (Akagi, 2013).

3.2.2. Phase partitioning by sequential extraction

In the sequential leaching procedure, the concentration of exchangeable phase REEs (extracted in Step 1) accounted for less than 1% of the total sedimentary REE inventory. The leached concentrations of Fe and Mn were negligible, remaining below the detection limit (<0.01 mg L^{-1}) in most cases. The carbonate/apatite phase REEs (liberated in Step 2), accounting for 8–22% of the total, exhibited a PAAS-normalized pattern characterized by distinct MREE and HREE enrichment and a pronounced negative cerium (Ce) anomaly ($Ce/Ce^* = 0.50 \pm 0.11$). Fe and Mn concentrations in this phase were also negligible. Step 3 extracted easily reducible Fe-Mn oxides, which released 15–32% of total Mn and 8–16% of total Fe. The REEs extracted in this step accounted for 8–20% of the total, comparable to Step 2, but with a very different PAAS-normalized pattern: relatively flat with a significant positive Ce anomaly ($Ce/Ce^* = 1.64 \pm 0.20$). Step 4 (oxidizable fraction) dissolved 2.7–14.3% of total Fe and 42–55% of total Mn. The REEs released in this step were minor, constituting <5% of the bulk sediment total. In Step 5 (biogenic silica), Fe and Mn were below the ICP-MS quantification limit, and REEs constituted <5% of the bulk sediment total.

The carbonate/apatite phase (Step 2) shows a pronounced negative Ce anomaly and HREE enrichment. This pattern reflects seawater influence, where REEs were scavenged and then incorporated into authigenic carbonate and phosphate minerals (Liao et al., 2022). In contrast, the Fe-Mn oxide phase (Step 3) displays a positive Ce anomaly. This indicates Ce scavenging by Mn (and Fe) oxides, during which dissolved Ce^{3+} was adsorbed and oxidized to less soluble Ce^{4+} (Bau et al., 2014; Bau and Koschinsky, 2009). We detected no positive Eu anomaly in the Fe-Mn oxide phase ($Eu/Eu^* = 0.92–1.02$), indicating that submarine hydrothermal activity does not dominate Fe-Mn oxide burial in the study area. This agrees with the known behavior of hydrothermal systems, which typically produce a distinct positive Eu anomaly in vent fluids and associated precipitates (e.g. Rouxel et al., 2018; Azami et al., 2023).

The residual fraction contained the highest proportions of both Fe (67–83%) and ΣREE (50–78%), along with 13–34% of the total Mn (Supplementary Table S5). The characteristics of this fraction are consistent with findings from other marine sedimentary environments (e.g., Roy, 2015). The PAAS-normalized REE patterns of the residual fraction varied among stations. There is a clear latitudinal gradient: northern stations show greater HREE enrichment, while southern stations have flatter patterns. In northern stations, the residual fraction exhibits HREE enrichment, which contrasts with the typically flat patterns of Asian aeolian loess and instead resembles the flat to HREE-enriched signatures characteristic of Kuril–Kamchatka volcanic materials (Weber II et al., 1996, 1998).

The residual fraction shows a clear latitudinal gradient: northern stations have stronger HREE enrichment, while southern stations have flatter patterns. This is shown by the relationship between the La/Yb ratio and distance from the volcanic arc (Supplementary Fig. 1), which shows a broad positive trend ($R^2 = 0.628$, $p = 0.06$), consistent with La/Yb increasing from the more volcanogenic north (La/Yb = 4.60 for Station D7 surface) toward the more aeolian-influenced south (La/Yb = 11.32 for Station P1–31). This plot illustrates the overall shift in lithogenic provenance with increasing distance. Residual REE patterns for all stations are shown in Fig. 2c.

4. Discussion

4.1. Sediment source partitioning and burial fluxes

4.1.1. Lithogenic and biogenic-authigenic proportions

As described in Section 3.2, the bulk sediment composition and sequential leaching results provide the basis for source apportionment. We then used the approach in Section 2.6 to quantify the lithogenic and biogenic fractions. The results are summarized in Table 2, showing percentage contributions from FL-Th and FL-Residual REE approaches. There are clear spatial variations in source contributions. For the total lithogenic fraction (aeolian dust and volcanic material), stations farther south have a higher proportion of terrigenous material, with the highest value (~90%) at station E10. Volcanic contributions in the north are up to five times higher than in the south, while dust influence shows the opposite trend, with similar magnitude.

The distribution of biogenic and authigenic components follows a similar north–south gradient. At station D7, the northernmost site, the

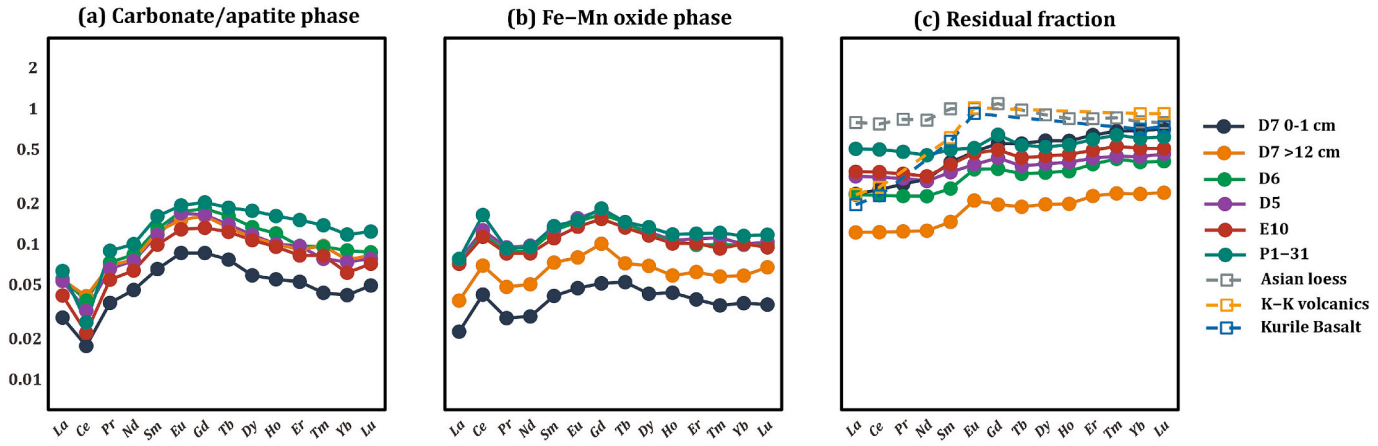


Fig. 2. PAAS-normalized REEs patterns for the major operationally defined phases extracted by sequential leaching: (a) carbonate/apatite phase; (b) Fe-Mn oxide phase; (c) residual aluminosilicate fraction.

Table 2
Source apportionment of bulk sediments: relative contributions (%) of Asian loess, volcanogenic material, and biogenic–authigenic components. FL denotes the lithogenic fraction, calculated from Al content. FL-Th and FL-Residue REEs denote two independent source-apportionment approaches for the lithogenic fraction: FL-Th uses Th concentrations, whereas FL-Residue REEs uses La/Yb ratios of the residual fraction. Values for Asian loess and volcanogenic material are expressed as percentages of the bulk sediment.

	FL-Th approaches		FL-Residue REEs approaches		
Station	Asian loess (%)	Volcanogenic material (%)	Asian loess (%)	Volcanogenic material (%)	Biogenic and authigenic particles (%)
D7 0-1cm	14 ± 4	58 ± 3	8 ± 4	63 ± 4	28 ± 5
D7 12–36 cm	8 ± 9	38 ± 11	16 ± 2	30 ± 2	54 ± 5
D6	28 ± 5	29 ± 5	24 ± 2	32 ± 2	43 ± 8
D5	53 ± 4	28 ± 4	35 ± 1	47 ± 1	18 ± 2
E10	42 ± 7	49 ± 6	46 ± 1	45 ± 1	9 ± 2
P1–31	60 ± 6	21 ± 4	64 ± 1	16 ± 1	19 ± 9

deeper section (>12 cm) contained the highest proportion (54%). Stations in the north, which have higher productivity, also contain a greater proportion of biogenic and authigenic components. This proportion is positively correlated with satellite-derived surface chlorophyll-a concentrations (r = 0.95; data from Hong et al., 2023), suggesting that higher primary productivity enhances the preservation and burial of these components.

We used two methods to quantify the dust and volcanic fractions within the lithogenic fraction: the Th approach and the residual-phase REE approach (Table 2). The two methods generally agree (r = 0.89 for loess fractions), but scatter at individual stations (e.g., D5) highlights the difficulty of separating volcanic and aeolian signals in mixed systems. This likely reflects uncertainties in end-member compositions and the different behavior of Th and REEs during transport and diagenesis.

Furthermore, the coarse bulk grain size does not affect the dust end-member used above. Although bulk sediments at the northernmost Station D7 show coarser grain-size distributions (e.g., 14–46 μm, with some layers containing particles <75 μm), this is a well-known feature of the highly productive, arc-proximal Northwest Pacific. Regional studies indicate that coarse particles in this area are dominated by large biogenic siliceous tests (e.g., large diatoms; Onodera et al., 2005), as well as proximal coarse volcanic ash, pumice, and ice-rafted debris (Scudder et al., 2016). This evidence indicates that the coarser bulk grain size reflects high biogenic productivity and local volcanic input, rather than anomalously coarse aeolian dust. Because aerodynamic sorting restricts the long-range transported aeolian component in this remote pelagic region to the fine-grained fraction (Maeda et al., 2007), our use of a fine-grained aeolian end-member remains robust and is unaffected by the coarse biogenic and volcanogenic components.

4.1.2. *Spatial variability in component burial fluxes*

Burial fluxes for each component (Table 3) were calculated by multiplying the mass flux (Section *3.1*) by the relative contributions from source apportionment (Section 4.1.1).

The dust flux we derived (0.18–0.25 g cm^{-2} ka^{-1}) is consistent with atmospheric model predictions (Mahowald et al., 2005), independent studies of dust in the Subarctic North Pacific (0.04–0.38 g cm^{-2} ka^{-1}, Serno et al., 2014a), and the Japanese aerosol reanalysis dataset (JRAero; Yumimoto et al., 2017). This consistency reflects the long-distance transport of dust from Central Asia and aligns with the expected exponential eastward decline in Asian dust transport (e.g., Zhang et al., 2016).

Volcanogenic material fluxes show a pronounced latitudinal gradient, with much higher values in the north. These estimates agree with values reported for the Izu-Bonin-Mariana Arc (Scudder et al., 2009, 2014) and for the Subarctic North Pacific (Serno et al., 2014a). High volcanic fluxes at northern stations (D6, D7) come from nearby Kuril–Kamchatka and Aleutian arc sources, together with transport by subarctic North Pacific circulation (Oyashio Current; Nishioka et al.,

Table 3
Burial fluxes of sediment components (g cm^{-2} ka^{-1}).

Station	Asian loess	Volcanogenic material	Biogenic and authigenic particles
D7 0-1cm	0.23	1.72	0.75
D7 12–36 cm	0.18	0.33	0.59
D6	0.20	0.27	0.35
D5	0.21	0.28	0.11
E10	0.21	0.21	0.04
P1–31	0.25	0.06	0.07

2020), which carries suspended volcaniclastic particles into the subarctic and transition zones. The southward spread of these particles is largely limited by the Kuroshio Extension front: although eddies and mixing allow some cross-frontal exchange, the front acts as a dynamic barrier that restricts direct southward penetration of Oyashio-sourced volcanic material into the subtropical gyre.

In contrast, southern stations (E10, P1–31) are farther from northern volcanic arcs and lie within the subtropical recirculation gyre. Shielded from northern volcanic inputs by the Kuroshio Extension front, this region receives terrigenous material mainly through atmospheric deposition. Asian dust, carried by the East Asian monsoon and mid-latitude westerly jet, is transported across the North Pacific and forms a basin-wide aeolian background flux (Serno et al., 2014a; Xu et al., 2014, 2015; Yumimoto et al., 2017).

Furthermore, volcanogenic flux shows a strong positive correlation with biogenic–authigenic flux (r = 0.78; Fig. 3), and both follow a similar latitudinal pattern. The higher biogenic–authigenic flux in the north reflects enhanced biological productivity, which is fueled by lithogenic nutrient supply (Lam and Bishop, 2008). It also reflects favorable conditions for the export and burial of biogenic particles (Honjo et al., 2008).

4.2. Mechanisms controlling biological export and trace metal burial

4.2.1. Linking volcanic inputs to enhanced biological production

Fe burial flux is more closely associated with volcanogenic input (r = 0.81) across our study transect. In the northern cores (D7, D6), where volcanic fluxes are highest (0.27–1.72 g cm^{-2} ka^{-1}), Fe burial reaches its maximum values; in contrast, the southern cores (E10, P1–31) receive lower volcanic inputs (0.06–0.21 g cm^{-2} ka^{-1}) and exhibit correspondingly lower Fe burial. This spatial pattern suggests that volcanic materials serve as the dominant local Fe source supporting elevated primary productivity in the Kuroshio Extension, particularly in the northern, arc-proximal sector. Aeolian dust, despite its weaker correlation, likely provides a regionally pervasive background Fe supply across the study area.

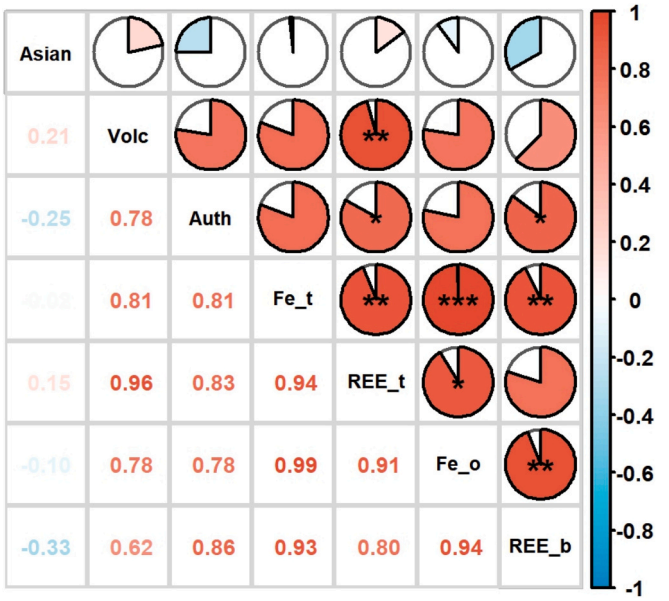


Fig. 3. Correlation matrix of burial fluxes for three sediment components (Asian loess, volcanogenic material, and biogenic–authigenic components) and four metal fluxes (total Fe, total REEs, Fe-Mn oxide-bound Fe, and biogenic–authigenic REEs). The variables are abbreviated as Asian, Volc, Auth, Fe_t, REEs_t, Fe_o, and REEs_b, respectively. The area of the pie chart sector is proportional to the magnitude of the Pearson correlation coefficient, with colors ranging from red (positive correlation) to blue (negative correlation). *, **, and *** indicate significant correlations at *p* < 0.05, *p* < 0.01, and *p* < 0.001, respectively. (For interpretation of the references to colour in this figure legend, the reader is referred to the web version of this article.)

The burial flux of non-residual Fe, especially the fraction associated with Fe-Mn oxides, also shows strong positive correlations with both volcanogenic flux and biogenic–authigenic flux (Fig. 3). These relationships are consistent with the well-established paradigm in high-nutrient, low-chlorophyll (HNLC) regions, where Fe availability is widely recognized as a primary limiting factor for phytoplankton growth (Martin and Fitzwater, 1988; Boyd et al., 2007). In the subarctic Pacific, proximal volcanic inputs have been repeatedly documented as an effective source of bioavailable Fe capable of alleviating nutrient limitation and stimulating biological productivity (Lam and Bishop, 2008; Hamme et al., 2010; Olgun et al., 2011). Our observations align with these regional and global syntheses, supporting a tight coupling between Fe cycling and the biological pump. Bioavailable Fe released from volcanic materials likely enhances phytoplankton growth and particulate organic carbon export, while the subsequent settling of biogenic particles acts as a critical carrier, facilitating the efficient transport of Fe from surface waters to the deep ocean for long-term sequestration.

4.2.2. Biogenic–mediated burial of REEs

A similar coupling pattern is observed for REEs. Both total and biogenic–authigenic REEs burial fluxes exhibit strong positive correlations with the burial flux of biogenic–authigenic components. Although the relative proportion of REEs hosted in the residual phase is lower in northern sediments, the absolute burial fluxes of REEs are substantially higher in the northern region. For instance, the total REEs burial flux at Station D7 is approximately 2.5 times that at Station P1–31. These observations indicate that the Kuroshio Extension acts as a significant sink for REEs, with biogenic and authigenic pathways playing a dominant role in removing these elements from the upper ocean.

Proximal volcanic Fe input may have enhanced biological export against a background of relatively refractory lithogenic input from aeolian dust. This may have strengthened the particle carrier effect and contributed to REE co-sequestration. The bioavailability of volcanic Fe depends on ash composition, age, and depositional environment, and direct measurements are still needed to confirm this pathway (Chen et al., 2020). This mechanism highlights the interconnected roles of lithogenic inputs and biological processes in regulating trace metal cycling in this dynamic oceanic region.

5. Implications

Our results suggest a positive feedback mechanism linking volcanic Fe supply, biological export, and trace metal burial (Fig. 4). Aeolian dust provides a regionally uniform background input (Xu et al., 2014; Serno et al., 2014a), while volcanic materials deliver a more localized but potent source (Lam and Bishop, 2008; Nishioka et al., 2020) of bioavailable Fe. Together, they alleviate Fe limitation, stimulate primary productivity (Browning et al., 2014), and enhance the export and burial of biogenic particles (Honjo et al., 2008; Sunda, 2012), which in turn facilitate the co-sequestration of trace metals such as REEs (Cao et al., 2024; Du et al., 2025).

However, we acknowledge that the proposed “Fe fertilization” mechanism remains inferential at this stage. Direct measurements of bioavailable Fe (e.g., dissolved Fe or ascorbate-extractable Fe) in the water column or porewaters are needed to confirm this pathway. Nonetheless, the strong spatial correlations we observed, together with the consistency with previous Fe-addition experiments (e.g., Boyd et al., 2007; Guan et al., 2026), support the plausibility of this interpretation. Future work should focus on quantifying the bioavailability of volcanic Fe and its impact on phytoplankton communities in this region.

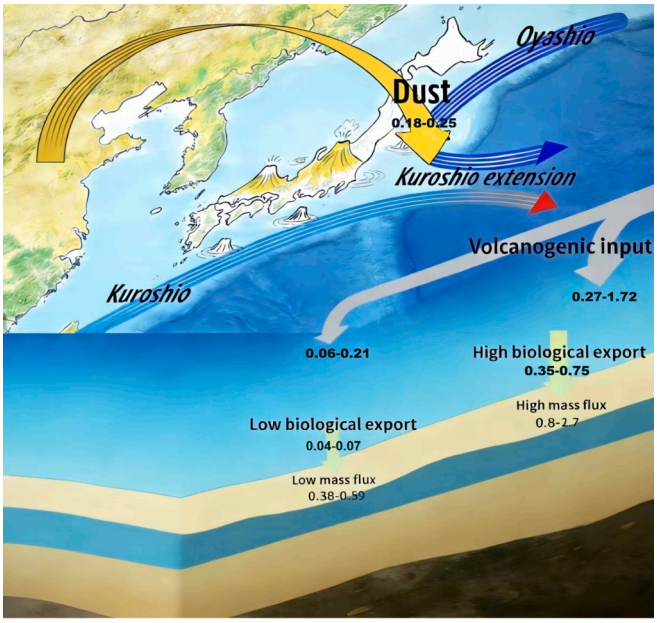


Fig. 4. Schematic diagram of enhanced biological export driven by aeolian dust and volcanic inputs (all flux units are g cm^{-2} ka^{-1}).

6. Conclusions

This study quantifies the burial fluxes and provenance of sedimentary materials across a north–south transect in the Kuroshio Extension. Mass fluxes show a pronounced north-to-south gradient, decreasing from 2.7 g cm^{-2} ka^{-1} in the north to 0.38 g cm^{-2} ka^{-1} in the south, a ~ 7-fold decrease from north to south. Aeolian dust provides a regionally uniform background flux (0.18–0.25 g cm^{-2} ka^{-1}), whereas volcanic inputs are more localized but more potent, with fluxes up to 1.72 g cm^{-2} ka^{-1} in the north and much lower values in the south. Elevated volcanic fluxes coincide spatially with enhanced biogenic particle burial (r = 0.78), suggesting that volcanic Fe fertilization stimulates biological export and promotes co-sequestration of trace metals such as REEs. Collectively, these findings highlight the interconnected roles of aeolian and volcanic inputs in regulating metal cycling and biological productivity in this dynamic oceanic region.

CRediT authorship contribution statement

Zenghui Zhu: Writing – original draft, Visualization, Methodology, Investigation. **Pinghe Cai:** Writing – review & editing, Methodology. **Qian Liu:** Supervision, Resources, Methodology. **Wen Liu:** Writing – review & editing, Visualization. **Xueyan Jiang:** Writing – review & editing, Resources. **Xiaoyi Guo:** Writing – review & editing. **Shibin Zhao:** Writing – review & editing. **Wenkai Guan:** Writing – review & editing, Resources. **Honghai Zhang:** Supervision, Resources, Investigation. **Guangchao Zhuang:** Resources. **Ergang Lian:** Writing – review & editing. **Shuo Ren:** Investigation. **Ran An:** Investigation. **Shanshan Chen:** Writing – review & editing. **Zhaohui Chen:** Resources. **Bochao Xu:** Writing – review & editing, Supervision, Funding acquisition, Conceptualization.

Declaration of competing interest

The authors declare that they have no known competing financial interests or personal relationships that could have appeared to influence the work reported in this paper.

Acknowledgments

This work was financially supported by the National Natural Science Foundation of China (nos. 42425602 and U22A20580), Shandong Provincial Natural Science Foundation (nos. 2025GJJLJRC-003), Special Projects of Frontiers Science Center for Deep Ocean Multispheres and Earth System (202672009), and the Fundamental Research Funds for the Central Universities (nos., 202561021, 202272001 and 202472001). We thank the captain and crews of the R/V "*dongfanghong 3*" for their assistance and cooperation during the investigation. Data and samples were collected onboard of R/V *dongfanghong 3* implementing the open research cruise NORC2024-584 supported by NSFC Shiptime Sharing Profect (42349584), the Laoshan Laboratory (LSKJ202400202).

Appendix A. Supplementary data

Supplementary data to this article can be found online at https://doi.org/10.1016/j.chemgeo.2026.123744.

Data availability

Data are available through Zenodo at https://zenodo.org/records/19393755

References

Akagi, T., 2013. Rare earth element (REE)–silicic acid complexes in seawater to explain the incorporation of REEs in opal and the "leftover" REEs in surface water: new interpretation of dissolved REE distribution profiles. Geochim. Cosmochim. Acta 113, 174–192. https://doi.org/10.1016/j.gca.2013.03.014.

Anderson, R.F., Fleer, A.P., 1982. Determination of natural actinides and plutonium in marine particulate material. Anal. Chem. 54, 1142–1147. https://doi.org/10.1021/ac00244a030.

Azami, K., Machida, S., Hirano, N., Nakamura, K., Yasukawa, K., Kogiso, T., Kato, Y., 2023. Hydrothermal ferromanganese oxides around a petit-spot volcano on old and cold oceanic crust. Commun. Earth Environ. 4, 191. https://doi.org/10.1038/s43247-023-00832-3.

Bacon, M.P., Anderson, R.F., 1982. Distribution of thorium isotopes between dissolved and particulate forms in the deep sea. J. Geophys. Res. Oceans 87, 2045–2056. https://doi.org/10.1029/jc087ic03p02045.

Bailey, J.C., 1993. Geochemical history of sediments in the northwestern Pacific Ocean. Geochem. J. 27, 71–90. https://doi.org/10.2343/geochemj.27.71.

Bau, M., Koschinsky, A., 2009. Oxidative scavenging of cerium on hydrous Fe oxide: evidence from the distribution of rare earth elements and yttrium between Fe oxides and Mn oxides in hydrogenetic ferromanganese crusts. Geochem. J. 43, 37–47. https://doi.org/10.2343/geochemj.1.0005.

Bau, M., Schmidt, K., Koschinsky, A., Hein, J., Kuhn, T., Usui, A., 2014. Discriminating between different genetic types of marine ferro-manganese crusts and nodules based on rare earth elements and yttrium. Chem. Geol. 381, 1–9. https://doi.org/10.1016/j.chemgeo.2014.05.004.

Boyd, P.W., Jickells, T., Law, C.S., Blain, S., Boyle, E.A., Buesseler, K.O., Coale, K.H., Cullen, J.J., de Baar, H.J.W., Follows, M., Harvey, M., Lancelot, C., Levasseur, M., Owens, N.P.J., Pollard, R., Rivkin, R.B., Sarmiento, J., Schoemann, V., Smetacek, V., Takeda, S., Tsuda, A., Turner, S., Watson, A.J., 2007. Mesoscale iron enrichment experiments 1993–2005: synthesis and future directions. Science 315, 612–617. https://doi.org/10.1126/science.1131669.

Browning, T.J., Bouman, H.A., Moore, C.M., Schlosser, C., Tarran, G.A., Woodward, E.M. S., Henderson, G.M., 2014. Nutrient regimes control phytoplankton ecophysiology in the South Atlantic. Biogeosciences 11, 463–479. https://doi.org/10.5194/bg-11-463-2014.

Burgay, F., Spolaor, A., Gabrieli, J., Cozzi, G., Turetta, C., Vallelonga, P., Barbante, C., 2021. Atmospheric iron supply and marine productivity in the glacial North Pacific Ocean. Clim. Past 17, 491–505. https://doi.org/10.5194/cp-17-491-2021.

Cao, A., Liu, Q., Zhang, J., Shiller, A.M., Cai, Y., Zhang, R., Liu, Z., 2024. Dissolved rare earth elements in the North Pacific Subtropical Gyre: lithogenic sources and water mass mixing control. Geochim. Cosmochim. Acta 372, 42–61. https://doi.org/10.1016/j.gca.2024.02.018.

Censi, P., Sprovieri, M., Saiano, F., Di Geronimo, S.I., Larocca, D., Placenti, F., 2007. The behaviour of REEs in Thailand's Mae Klong estuary: suggestions from the Y/Ho ratios and lanthanide tetrad effects. Estuar. Coast. Shelf Sci. 71, 569–579. https://doi.org/10.1016/j.ecss.2006.09.003.

Chen, T., Liu, Q., Roberts, A., Shi, X., Zhang, Q., 2020. A test of the relative importance of iron fertilization from aeolian dust and volcanic ash in the stratified high-nitrate low-chlorophyll subarctic Pacific Ocean. Quat. Sci. Rev. 248, 106577. https://doi.org/10.1016/j.quascirev.2020.106577.

Cheng, Y., Cai, P., Chen, H., Yuan, L., Jiang, X., Zhang, S., Sohrin, Y., 2024. Nitrate and silicate fluxes at the sediment–water interface of the deep North Pacific Ocean

illuminated by $^{226}Ra/^{230}Th$ disequilibria. Geochim. Cosmochim. Acta 383, 81–91. https://doi.org/10.1016/j.gca.2024.08.008.
Cochran, J.K., Krishnaswami, S., 1980. Radium, thorium, uranium, and ^{210}Pb in deep-sea sediments and sediment pore waters from the North Equatorial Pacific. Am. J. Sci. 280, 849–889. https://doi.org/10.2475/ajs.280.9.849.
Costa, K.M., Hayes, C.T., Anderson, R.F., Pavia, F.J., Bausch, A., Deng, F., Dutay, J.C., Geibert, W., Heinze, C., Henderson, G., Hillaire-Marcel, C., Hoffmann, S., Jaccard, S. L., Jacobel, A.W., Kienast, S.S., Kipp, L., Lerner, P., Lippold, J., Lund, D., Marcantonio, F., McGee, D., McManus, J.F., Mekik, F., Middleton, J.L., Missiaen, L., Not, C., Pichat, S., Robinson, L.F., Rowland, G.H., Roy-Barman, M., Tagliabue, A., Torfstein, A., Winckler, G., Zhou, Y., 2020. 230Th normalization: new insights on an essential tool for quantifying sedimentary fluxes in the modern and Quaternary Ocean. Paleoceanogr. Paleoclimatol. 35, e2019PA003820. https://doi.org/10.1029/2019PA003820.
Costa, K.M., Pavia, F.J., Piecuch, C.G., McManus, J.F., Weinstein, G.A., 2024. Pelagic sedimentation rates in the North Pacific using Thorium-230 depth profiling. Geochim. Cosmochim. Acta 369, 126–140. https://doi.org/10.1016/j.gca.2023.11.020.
Crusius, J., Lao, C.A., Holmes, T.M., Murray, J.W., 2024. Alaskan glacial dust is an important iron source to surface waters of the Gulf of Alaska. Geophys. Res. Lett. 51, e2023GL106778. https://doi.org/10.1029/2023GL106778.
Du, J., Haley, B.A., McManus, J., Blaser, P., Rickli, J., Vance, D., 2025. Abyssal seafloor as a key driver of ocean trace-metal biogeochemical cycles. Nature 642, 620–627. https://doi.org/10.1038/s41586-025-09038-3.
Duce, R.A., Liss, P.S., Merrill, J.T., Atlas, E.L., Buat-Menard, P., Hicks, B.B., Miller, J.M., Prospero, J.M., Arimoto, R., Church, T.M., Ellis, W., Galloway, J.N., Hansen, L., Jickells, T.D., Knap, A.H., Reinhardt, K.H., Schneider, B., Soudine, A., Tokos, J.J., Tsunogai, S., Wollast, R., Zhou, M., 1991. The atmospheric input of trace species to the world ocean. Glob. Biogeochem. Cycles 5, 193–259. https://doi.org/10.1029/91gb01778.
Francois, R., Frank, M., Rutgers van der Loeff, M.M., Bacon, M.P., 2004. ^{230}Th normalization: an essential tool for interpreting sedimentary fluxes during the late Quaternary. Paleoceanography 19, PA1018. https://doi.org/10.1029/2003PA000939.
Geibert, W., Stimac, I., Rutgers van der Loeff, M.M., Kuhn, G., 2019. Dating deep-sea sediments with ^{230}Th excess using a constant rate of supply model. Paleoceanogr. Paleoclimatol. 34, 1895–1912. https://doi.org/10.1029/2019PA003663.
Guan, W., Lan, M., Lee, Y.P., Huang, Y., Lin, H., Chen, M., Zhang, R., 2026. Trace elements in Arctic Ocean aerosols: contemporary status and decadal variability. J. Geophys. Res. Atmos. 131, e2025JD045561. https://doi.org/10.1029/2025JD045561.
Hamme, R.C., Webley, P.W., Crawford, W.R., Whitney, F.A., DeGrandpre, M.D., Emerson, S.R., Eriksen, C.C., Giesbrecht, K.E., Gower, J.F.R., Kavanaugh, M.T., Peña, M.A., Sabine, C.L., Batten, S.D., Coogan, L.A., Grundle, D.S., Lockwood, D., 2010. Volcanic ash fuels anomalous plankton bloom in subarctic northeast Pacific. Geophys. Res. Lett. 37, L19604. https://doi.org/10.1029/2010gl044629.
Hayes, C.T., Costa, K.M., Anderson, R.F., Calvo, E., Chase, Z., Demina, L.L., Dutay, J.C., German, C.R., Heimburger-Boavida, L.E., Jaccard, S.L., Jacobel, A., Kohfeld, K.E., Kravchishina, M.D., Lippold, J., Mekik, F., Missiaen, L., Pavia, F.J., Paytan, A., Pedrosa-Pamies, R., Petrova, M.V., Rahman, S., Robinson, L.F., Roy-Barman, M., Sanchez-Vidal, A., Shiller, A., Tagliabue, A., Tessin, A.C., van Hulten, M., Zhang, J., 2021. Global Ocean sediment composition and burial flux in the deep sea. Glob. Biogeochem. Cycles 35, e2020GB006769. https://doi.org/10.1029/2020gb006769.
Hong, Z., Long, D., Li, X., Wang, Y., Zhang, J., Hamouda, M.A., Mohamed, M.M., 2023. A global daily gap-filled chlorophyll-a dataset in open oceans during 2001–2021 from multisource information using convolutional neural networks. Earth Syst. Sci. Data 15, 5281–5300. https://doi.org/10.5194/essd-15-5281-2023.
Honjo, S., Manganini, S.J., Krishfield, R.A., Francois, R., 2008. Particulate organic carbon fluxes to the ocean interior and factors controlling the biological pump: a synthesis of global sediment trap programs since 1983. Prog. Oceanogr. 76, 217–285. https://doi.org/10.1016/j.pocean.2007.11.003.
Jeong, G. Y. (2020). Mineralogy and geochemistry of Asian dust: dependence on migration path, fractionation, and reactions with polluted air. Atmos. Chem. Phys., 20(12), 7411-7428. Doi:https://doi.org/10.5194/acp-20-7411-2020.
Jiang, F., Frank, M., Li, T., Chen, T.Y., Xu, Z., Li, A., 2013. Asian dust input in the western Philippine Sea: evidence from radiogenic Sr and Nd isotopes. Geochem. Geophys. Geosyst. 14, 1538–1551. https://doi.org/10.1002/ggge.20116.
Kay, R.W., 1977. Geochemical constraints on the origin of Aleutian magmas. In: Talwani, M., Pittman, W.C. Ill (Eds.), Island Arcs, Deep Sea Trenches and Back Arc Basins: Am. Geophys. Union, Maurice Ewing Sen, 1, pp. 229–242.
Koschinsky, A., Halbach, P., 1995. Sequential leaching of marine ferromanganese precipitates: genetic implications. Geochim. Cosmochim. Acta 59, 5113–5132. https://doi.org/10.1016/0016-7037(95)00358-4.
Kurisu, M., Sakata, K., Uematsu, M., Ito, A., Takahashi, Y., 2021. Contribution of combustion Fe in marine aerosols over the northwestern Pacific estimated by Fe stable isotope ratios. Atmos. Chem. Phys. 21, 16027–16050. https://doi.org/10.5194/acp-21-16027-2021.
Lam, P.J., Bishop, J.K., 2008. The continental margin is a key source of iron to the HNLC North Pacific Ocean. Geophys. Res. Lett. 35, L07608. https://doi.org/10.1029/2008gl033294.
Lam, P.J., Ohnemus, D.C., Marcus, M.A., 2012. The speciation of marine particulate iron adjacent to active and passive continental margins. Geochim. Cosmochim. Acta 80, 108–124. https://doi.org/10.1016/j.gca.2011.11.044.
Lam, P.J., Robinson, L.F., Blusztajn, J., Li, C., Cook, M.S., McManus, J.F., Keigwin, L.D., 2013. Transient stratification as the cause of the North Pacific productivity spike during deglaciation. Nat. Geosci. 6, 622–626. https://doi.org/10.1038/ngeo1873.
Letelier, R.M., Björkman, K.M., Church, M.J., Hamilton, D.S., Mahowald, N.M., Scanza, R.A., Schneider, N., White, A.E., Karl, D.M., 2019. Climate-driven oscillation of phosphorus and iron limitation in the North Pacific Subtropical Gyre. Proc. Natl. Acad. Sci. USA 116, 12720–12728. https://doi.org/10.1073/pnas.1900789116.
Liao, J., Chen, J., Sun, X., Wu, Z., Deng, Y., Shi, X., Koschinsky, A., 2022. Quantifying the controlling mineral phases of rare-earth elements in deep-sea pelagic sediments. Chem. Geol. 595, 120792. https://doi.org/10.1016/j.chemgeo.2022.120792.
Maeda, N., Noriki, S., Narita, H., 2007. Grain size, La/Yb and Th/Sc of settling particles in the western North Pacific: evidence for lateral transport of small Asian loess. J. Oceanogr. 63, 803–812. https://doi.org/10.1007/s10872-007-0068-8.
Mahowald, N.M., Baker, A.R., Bergametti, G., Brooks, N., Duce, R.A., Jickells, T.D., Kubilay, N., Prospero, J.M., Tegen, I., 2005. Atmospheric global dust cycle and iron inputs to the ocean. Glob. Biogeochem. Cycles 19, GB4025. https://doi.org/10.1029/2004gb002402.
Mahowald, N.M., Hamilton, D.S., Mackey, K.R., Moore, J.K., Baker, A.R., Scanza, R.A., Zhang, Y., 2018. Aerosol trace metal leaching and impacts on marine microorganisms. Nat. Commun. 9, 2614. https://doi.org/10.1038/s41467-018-04970-7.
Martin, J.H., Fitzwater, S.E., 1988. Iron deficiency limits phytoplankton growth in the north-east Pacific subarctic. Nature 331, 341–343. https://doi.org/10.1038/331341a0.
McGee, D., Winckler, G., Borunda, A., Serno, S., Anderson, R.F., Recasens, C., Bory, A., Gaiero, D., Jaccard, S., Kaplan, M., McManus, M., Revel, M., Sun, Y., 2016. Tracking eolian dust with helium and thorium: impacts of grain size and provenance. Geochim. Cosmochim. Acta 175, 47–67. https://doi.org/10.1016/j.gca.2015.11.023.
McKay, J.L., Pedersen, T.F., 2008. The accumulation of silver in marine sediments: a link to biogenic Ba and marine productivity. Glob. Biogeochem. Cycles 22, GB4010. https://doi.org/10.1029/2007gb003136.
Nemati, K., Bakar, N.K.A., Abas, M.R., Sobhanzadeh, E., 2011. Speciation of heavy metals by modified BCR sequential extraction procedure in different depths of sediments from Sungai Buloh, Selangor, Malaysia. J. Hazard. Mater. 192, 402–410. https://doi.org/10.1016/j.jhazmat.2011.05.039.
Nishioka, J., Obata, H., Ogawa, H., Ono, K., Yamashita, Y., Lee, K., Takeda, S., Yasuda, I., 2020. Subpolar marginal seas fuel the North Pacific through the intermediate water at the termination of the global ocean circulation. Proc. Natl. Acad. Sci. USA 117, 12665–12673. https://doi.org/10.1073/pnas.2000658117.
Olgun, N., Duggen, S., Croot, P.L., Delmelle, P., Dietze, H., Schacht, U., Garbe-Schönberg, D., 2011. Surface Ocean iron fertilization: the role of airborne volcanic ash from subduction zone and hot spot volcanoes and related iron fluxes into the Pacific Ocean. Glob. Biogeochem. Cycles 25, GB4001. https://doi.org/10.1029/2009gb003761.
Olivarez, A.M., Owen, R.M., Rea, D.K., 1991. Geochemistry of eolian dust in Pacific pelagic sediments: Implications for paleoclimatic interpretations. Geochim. Cosmochim. Acta 55, 2147–2158. https://doi.org/10.1016/0016-7037(91)90093-k.
Onodera, J., Takahashi, K., Honda, M.C., 2005. Pelagic and coastal diatom fluxes and the environmental changes in the northwestern North Pacific during December 1997–May 2000. Deep-Sea Res. Pt. II 52 (16–18), 2218–2239. https://doi.org/10.1016/j.dsr2.2005.07.005.
Otosaka, S., Honda, M.C., Noriki, S., 2004. La/Yb and Th/Sc in settling particles: Vertical and horizontal transport of lithogenic material in the western North Pacific. Geochem. J. 38, 515–525. https://doi.org/10.2343/geochemj.38.515.
Rouxel, O., Toner, B., Germain, Y., Glazer, B., 2018. Geochemical and iron isotopic insights into hydrothermal iron oxyhydroxide deposit formation at Loihi Seamount. Geochim. Cosmochim. Acta 220, 449–482.
Roy, A., 2015. Biogeochemical Study of Trace Elements in Surface Sediment from the Marginal Sea (East China Sea) to the Open-Ocean (Northwestern Pacific). Doctoral Dissertation. University of Toyama, Toyama.
Rudnick, R.L., Gao, S., 2014. Composition of the continental crust. In: Holland, H.D., Turekian, K.K. (Eds.), Treatise on Geochemistry, 2nd ed. vol. 4. Elsevier, pp. 1–51. https://doi.org/10.1016/B978-0-08-095975-7.00301-6.
Sanchez-Cabeza, J.A., Ruiz-Fernández, A.C., 2012. ^{210}Pb sediment radiochronology: an integrated formulation and classification of dating models. Geochim. Cosmochim. Acta 82, 183–200. https://doi.org/10.1016/j.gca.2010.12.024.
Scudder, R.P., Murray, R.W., Plank, T., 2009. Dispersed ash in deeply buried sediment from the northwest Pacific Ocean: an example from the Izu–Bonin arc (ODP Site 1149). Earth Planet. Sci. Lett. 284, 639–648. https://doi.org/10.1016/j.epsl.2009.05.037.
Scudder, R.P., Murray, R.W., Schindlbeck, J.C., Kutterolf, S., Hauff, F., McKinley, C.C., 2014. Regional-scale input of dispersed and discrete volcanic ash to the Izu-Bonin and Mariana subduction zones. Geochem. Geophys. Geosyst. 15, 4369–4379. https://doi.org/10.1002/2014GC005561.
Scudder, R.P., Murray, R.W., Schindlbeck, J.C., Kutterolf, S., Hauff, F., Underwood, M.B., McKinley, C.C., 2016. Geochemical approaches to the quantification of dispersed volcanic ash in marine sediment. Prog. Earth Planet Sci. 3, 1. https://doi.org/10.1186/s40645-015-0077-y.
Seo, I., Lee, Y.I., Yoo, C.M., Kim, H.J., Hyeong, K., 2014. Sr-Nd isotope composition and clay mineral assemblages in eolian dust from the central Philippine Sea over the last 600 kyr: implications for the transport mechanism of Asian dust. J. Geophys. Res. Atmos. 119, 11492–11504. https://doi.org/10.1002/2014JD022025.
Serno, S., Winckler, G., Anderson, R.F., Hayes, C.T., McGee, D., Machalett, B., Ren, H., Straub, S.M., Gersonde, R., Haug, G.H., 2014a. Eolian dust input to the Subarctic North Pacific. Earth Planet. Sci. Lett. 387, 252–263. https://doi.org/10.1016/j.epsl.2013.11.008.
Serno, S., Winckler, G., Anderson, R.F., Hayes, C.T., Ren, H., Gersonde, R., Haug, G.H., 2014b. Using the natural spatial pattern of marine productivity in the Subarctic

North Pacific to evaluate paleoproductivity proxies. Paleoceanography 29, 438–453. https://doi.org/10.1002/2013PA002594.

Shigemitsu, M., Narita, H., Watanabe, Y.W., Harada, N., Tsunogai, S., 2007. Ba, Si, U, Al, Sc, La, Th, C and $^{13}C/^{12}C$ in a sediment core in the western subarctic Pacific as proxies of past biological production. Mar. Chem. 106, 442–455. https://doi.org/10.1016/j.marchem.2007.04.004.

Sunda, W.G., 2012. Feedback interactions between trace metal nutrients and phytoplankton in the ocean. Front. Microbiol. 3, 204. https://doi.org/10.3389/fmicb.2012.00204.

Taylor, S.R., McLennan, S.M., 1985. The Continental Crust: Its Composition and Evolution. Blackwell Scientific Publications, Oxford.

Tessier, A., Campbell, P.G.C., Bisson, M., 1979. Sequential extraction procedure for the speciation of particulate trace metals. Anal. Chem. 51, 844–851. https://doi.org/10.1021/ac50043a017.

Wang, P., Deng, Y., Zhang, G., Liu, D., Ma, J., Liu, C., Chen, F., 2025a. Impact of iron biogeochemical cycling in deep-sea environments on rare earth element enrichment. Chem. Geol. 692, 122951. https://doi.org/10.1016/j.chemgeo.2025.122951.

Wang, X., Zhang, X., Yang, W., Shi, D., Chen, M., Cheng, H., Cai, Y., 2025b. Dust deposition and iron cycling in the tropical western North Pacific based on thorium supply. Glob. Planet. Chang. 247, 104740. https://doi.org/10.1016/j.gloplacha.2025.104740.

Weber II, E.T., Owen, R.M., Dickens, G.R., Halliday, A.N., Jones, C.E., Rea, D.K., 1996. Quantitative resolution of eolian continental crustal material and volcanic detritus in North Pacific surface sediment. Paleoceanography 11, 115–127. https://doi.org/10.1029/95pa02720.

Weber II, E.T., Owen, R.M., Dickens, G.R., Rea, D.K., 1998. Causes and implications of the middle rare earth element depletion in the eolian component of North Pacific sediment. Geochim. Cosmochim. Acta 62, 1735–1744. https://doi.org/10.1016/s0016-7037(98)00102-1.

Xiao, T., Xu, D., Deng, T., Lin, J., Ye, L., Ge, Q., Chu, F., 2024. The influence of seamounts on the enrichment of rare earth elements in sediments—a case study of the Marcus-Wake Seamounts in the Western Pacific Ocean. J. Mar. Sci. Eng. 12, 117. https://doi.org/10.3390/jmse12010117.

Xu, Z., Li, T., Wan, S., Yin, X., Jiang, F., Sun, H., Lim, D., 2014. Geochemistry of rare earth elements in the mid-late Quaternary sediments of the western Philippine Sea and their paleoenvironmental significance. Sci. China Earth Sci. 57, 802–812. https://doi.org/10.1007/s11430-013-4786-z.

Xu, Z., Li, T., Clift, P.D., Lim, D., Wan, S., Chen, H., Xiong, Z., 2015. Quantitative estimates of Asian dust input to the western Philippine Sea in the mid-late Quaternary and its potential significance for paleoenvironment. Geochem. Geophys. Geosyst. 16, 3182–3196. https://doi.org/10.1002/2015gc005929.

Yang, H.S., Nozaki, Y., Sakai, H., Nagaya, Y., Nakamura, K., 1986. Natural and man-made radionuclide distributions in Northwest Pacific deep-sea sediments: rates of sedimentation, bioturbation and ^{226}Ra migration. Geochem. J. 20, 29–40. https://doi.org/10.2343/geochemj.20.29.

Yuan, L., Cai, P., Jiang, X., Geibert, W., Cheng, Y., Chen, Y., 2023. Precise measurement of $^{226}Ra/^{230}Th$ disequilibria in deep-sea sediments by high-sensitivity ICP-MS. Chem. Geol. 620, 121351. https://doi.org/10.1016/j.chemgeo.2023.121351.

Yumimoto, K., Tanaka, T.Y., Oshima, N., Maki, T., 2017. JRAero: the Japanese reanalysis for aerosol v1. 0. *Geoscientific Model*. Development 10 (9), 3225–3253.

Zan, J., Maher, B.A., Fang, X., Stevens, T., Ning, W., Wu, F., Hu, Z., 2025. Global dust impacts on biogeochemical cycles and climate. Nat. Rev. Earth Environ. https://doi.org/10.1038/s43017-025-00734-2.

Zhang, W., Chen, J., Ji, J., Li, G., 2016. Evolving flux of Asian dust in the North Pacific Ocean since the late Oligocene. Aeolian Res. 23, 11–20. https://doi.org/10.1016/j.aeolia.2016.09.004.

Zhao, W., Liu, L., Chen, J., Ji, J., 2019. Geochemical characterization of major elements in desert sediments and implications for the Chinese loess source. Sci. China Earth Sci. 62, 1428–1440. https://doi.org/10.1007/s11430-018-9354-y.

Zhu, Z., Yu, H., Bianchi, T.S., Lian, E., Burnett, W.C., Paytan, A., Xu, B., 2024. What causes excess deepening of the sediment mixed layer in the deep ocean? Geophys. Res. Lett. 51, e2024GL108928. https://doi.org/10.1029/2024GL108928.

Ziegler, C.L., Murray, R.W., Hovan, S.A., Rea, D.K., 2007. Resolving eolian, volcanogenic, and authigenic components in pelagic sediment from the Pacific Ocean. Earth Planet. Sci. Lett. 254, 416–432. https://doi.org/10.1016/j.epsl.2006.11.049.